Research Article

Fiber Formation of Printed Carbon Fiber/Poly (Ether Ether Ketone) with Different Nozzle Shapes

A Matschinski,[a]* P Ziegler,[a] T Abstreiter,[b] T Wolf[a] and K Drechsler[a]

Abstract

The additive manufacturing industry shows annual growth of more than 10 %. Therefore, the requirements for produced components are increasing, especially for individual medical technology applications printed from poly(ether ether ketone) (PEEK). This paper focuses on an investigation of an uninterrupted nozzle system for printing the high-performance thermoplastic PEEK with short fiber reinforcements. A custom-made nozzle design with variable outlet angle is presented and the achievable fiber length distribution and fiber orientation in the printed material are investigated. The applied nozzle angles are 60 °, 90 ° and 120 °. The geometric shape of the tip of the custom-made nozzles is comparable to that of a reference nozzle. With regard to the height profile, the inner surface is up to three times smoother. With a decreasing nozzle angle, a lower degree of fiber damage caused by deposition can be demonstrated. Thus, the process-induced shortening of the fibers decreases. The enhanced flow profile for small angles outweighs the simultaneous disadvantageous due to friction loss, shear stress and pressure drop. A clear result for the fiber orientation cannot be deduced.
© 2021 The Authors. *Polymer International* published by John Wiley & Sons Ltd on behalf of Society of Industrial Chemistry.

Keywords: additive manufacturing; fused filament fabrication; poly(ether ether ketone) (PEEK); nozzle shape; fiber orientation; fiber length

INTRODUCTION

The market segment of additive manufacturing shows an annual growth of more than 10 % since 2010[1]. One of the most important trends is the direct production of functional parts. Extrusion-based processes are very popular for this purpose[2]. They allow an easy insertion of fiber reinforcements without size limitations[3]. The possibility of printing high-performance polymers has further expanded the field of application for extrusion-based processes[4].

In the interior area of an Airbus A350 XWB, several thousand parts made of ULTEM 9085 are already in flight service[1]. However, the scope of use is limited to secondary structures within aircraft[5]. Moreover, ULTEM 9085 does not fulfill all requirements regarding chemical resistance. It is not resistant to some hydraulic fluids and dichloromethane that are used in aviation cleaning agents. This encourages a shift towards the application of poly(ether ether ketone) (PEEK) as a high-performance material. This material opens up additional fields of application, such as medical technology[6].

The requirements for individual medical technology applications of printed high-performance materials have already been developed[7]. Neat PEEK polymer has been successfully processed and evaluated in printed patient implants[8,9]. A wider range of use requires an improvement in mechanical properties. Adding short fibers can generate the required boost of the mechanical properties. An addition of 30 % short carbon fiber in weight raises strength from 100 to 260 MPa and Young's modulus from 3.7 to

25 GPa[10]. Cortical bone has a strength of 133 MPa and a stiffness of 18.6 GPa[11,12]. Therefore, the use of fiber-reinforced PEEK as bone substitute is possible from a mechanical point of view.

The addition of fibers turns a printing material into a heterogeneous material. At process temperature, PEEK has a viscosity of 0.5–1 kPas in unreinforced form. The added fiber material changes the extrusion behavior. A higher fiber content increases the viscosity[13,14]. With a higher viscosity, additional challenges for the processing of the filled material arise. In order to ensure high mechanical performance, the fibers must be as long as possible and aligned parallel to the direction of loading. The extrusion nozzle sits at the end of the liquefier and determines the extrusion geometry, and hence affects the mechanical properties significantly[15,16].

Regarding the geometrical classification of a nozzle, Turner *et al.*[16] divided the shape of a nozzle into three zones (Fig. 1). The first zone is a cylindrical section. It is slightly larger than the

* Correspondence to: A Matschinski, Chair of Carbon Composites, TUM Department of Aerospace and Geodesy, Technical University of Munich, Boltzmannstr. 15, 85748 Garching, Germany. E-mail: alexander.matschinski@tum.de

a Chair of Carbon Composites, TUM Department of Aerospace and Geodesy, Technical University of Munich, Garching, Germany

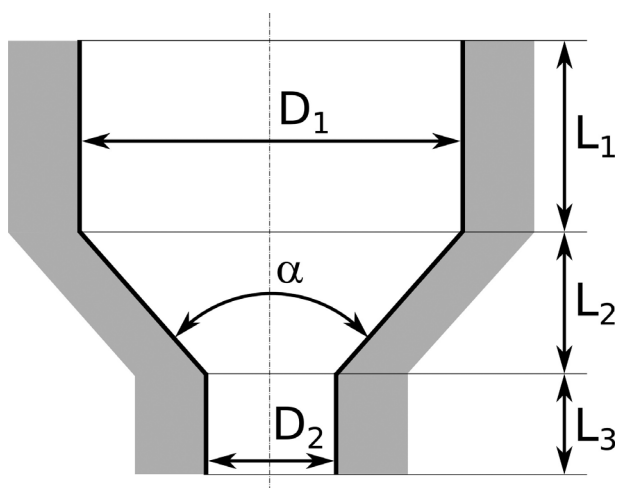b Chair of Astronautics, TUM Department of Aerospace and Geodesy, Technical University of Munich, Garching, Germany

Figure 1. Longitudinal section of a nozzle.[16]

filament. With a filament diameter of 1.75 mm, zone 1 usually has a diameter of 2 mm. Zone 1 is entirely in the area of the hot end. Upon entering this area, the filament is melted through heat conduction at extrusion temperature. Zone 2 consists of a conically convergent geometry, with an opening angle α. This is also known as the nozzle angle. The following nozzle outlet channel again consists of a cylindrical geometry. With lengths L_1, L_2 and L_3 and diameters D_1 and D_2, the geometry of the axisymmetric nozzle can be fully described[16,17]. A widely used standard is the nozzle geometry of E3D-online. A common nozzle angle is 120°. The standard outlet diameter is 0.4 mm. Thus, the reduction ratio is 5:1 (D_1/D_2). The reduction channel (zone 3) has a standard diameter to length ratio of *approx.* 1.5 (L_3/D_2).

During operation, continuous filament transport creates a constant melt flow[18]. The following solid filament acts like a piston and presses the already melted material through the nozzle outlet[19]. The deposition velocity for PEEK is usually below 60 mms^{-1} with a standard nozzle outlet. With an extrusion width of 0.4 mm and a layer height of 0.2 mm, the fluid velocity for the nozzle standard before constriction is below 1.5 mms^{-1}. The shear rate within this area is 100s^{-1} at its maximum[19], and the viscosity of PEEK at processing temperature is about 200 Pas[14].
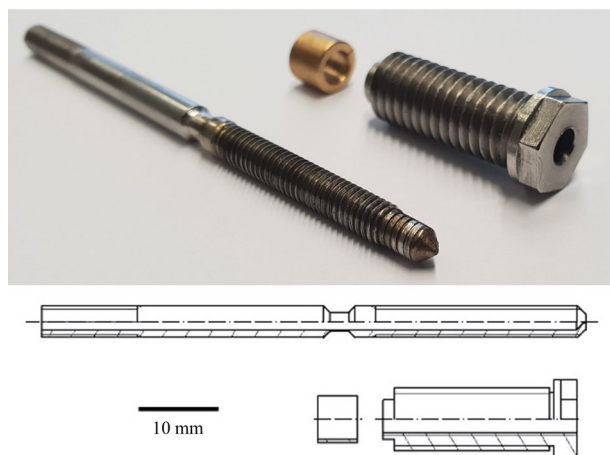

Figure 2. Nozzle adapter for mounting of custom-made nozzle inserts.

With these parameters, the following applies to the pipe flow:

$$Re = \frac{\rho \times \upsilon \times d}{\eta} \ll 1$$

Hence it is a Stokes flow[20]. The high contraction ratio of 5:1 towards the nozzle tip increases the Reynolds number, yet not out of the validity range. In this flow condition, the viscous forces outweigh the inertial forces. Furthermore, the constriction changes the pressure drop within the fluid. This must be counteracted by the feeding mechanism[18]. Gibson and Williamson[21] as well as Michaeli[22] have formulated the basics of the shear-thinning power-law fluid for the description of fluid behavior in nozzles. These basics are valid for the sections L_1 to L_3 separately and together they discribe the total pressure drop. Yardimci *et al.*[23] and Bellini[24] linked them with the boundary conditions of fused filament fabrication (FFF). Using the Arrhenius equation, Bellini *et al.*[18] created the following relationship for the cone section, which is also referred to by Ramanath *et al.*[25].

$$\Delta p_2 = \frac{2m}{3\tan(\alpha/2)} \left(\frac{1}{D_2^{3/m}} - \frac{1}{D_1^{3/m}} \right) \left(\left(\frac{D_1}{2} \right)^2 (m+3) + 2^{m+3} \right)^{1/m}$$
$$\exp \left[\alpha_1 \left(\frac{1}{T} - \frac{1}{T_\alpha} \right) \right]$$

where m is the material-dependent flow index[22], α_1 is the energy of activation and T_α is a reference temperature[18].

The predominant viscous forces in Stokes flow cause frictional losses, which increase with the nozzle length. A large nozzle angle can reduce the friction losses due to the change in the cross-sectional area over a short distance. As a result, cumulative shear stresses decrease with a large nozzle angle[23]. These shear forces occur at the transition from zone 2 (L_2) and zone 3 (L_3) as well as in the entire zone 3 (L_3). For a nozzle angle of 90°, Phan *et al.*[19] calculated a local shear rate of more than 800 s^{-1} at the inner wall in zone 3. Furthermore, the pressure drop decreases with an increasing nozzle angle in the cone section (see Δp_2). This is directly proportional to the counter-pressure of the nozzle. A decreasing pressure drop impedes the buckling or breaking of the filament at the inlet of the nozzle as well as possible slippage during the feeding of the filament[24]. Consequently, a larger nozzle angle leads to an improved performance and finally to a more uniform strand output[26]. At the same time, the constriction at large nozzle angles causes the fluid elements to lift off the inner wall of the barrel. The formation of recirculation areas is a consequence.[20] These areas of recirculation[27] are the so-called vortex[28] or dead water areas. This means that the polymer is held in a loop at undercuts by a vortex-like flow. In practical terms, these dead water areas can lead to the degradation of standing material[29]. These vortical regions make the processing of filled materials more difficult. The effects of these difficulties are flow instabilities and nozzle clogging[23]. As a result, the influence of the nozzle angle on the flow profile counteracts the influence of the friction loss, shear stress and pressure drop.

These physical factors of influence affect the additive manufacturing process at part level with regard to the quality and the fiber formation. This is one of the focuses of current research in additive manufacturing. The aforementioned physical factors lead to nozzle failure, which is the primary defect in extrusion based processes[30–33]. In additive manufacturing, this manifests as nozzle clogging[34,35]. Among other reasons, this leads to

a 20 % failure rate in FFF[36]. In addition to the physical factors of influence due to geometric dependencies, the surface of the nozzle inner wall has an influence on the extrusion. Chen et al.[37] and Kissi et al.[38] were able to establish a correlation between the nozzle wall properties and the extrusion quality. Chen et al. demonstrated a better wall sliding behavior with decreasing surface roughness. Kissi et al. generalized this result and demonstrated a better material flow for a given nozzle geometry by reducing surface roughness. In addition, Arda and Mackley[39] showed a correlation between the extrusion instability and the magnitude of the stress concentration at the nozzle exit. This correlation depends on both the melt/wall separation point as well as on the partial slip degree on the nozzle wall. Arda and Mackley[39] characterized these interactions by the degree of formation of a sharkskin on the extruded material surface. Based on this result, Agassant et al.[30] classified three polymer processing instabilities. Two of them are significantly influenced by the inner nozzle surface.

The addition of fibers changes the rheological behavior of the polymer inside the nozzle[40]. The phenomena mentioned increase in severity, and so do the processing challenges. A common feedstock material for FFF has a fiber mass content of 30 % and an average fiber length between 100 and 200 μm. Wang et al.[34] postulated a maximum fiber mass content of 40 % that can be processed without clogging. Besides the fiber content, the fiber length and orientation are crucial for the overall performance of a printed part[41]. Longer fibers in the printed part increase the mechanical performance[42].

Fu and Lauke[43] studied the influence of fiber length and orientation in short-fiber-reinforced polymers. They presented a validated model with a fiber efficiency factor that describes the strength of the composite. In short fiber reinforcements, the average fiber length is below the critical fiber length. Therefore, further shortening of the fibers has an excessive effect on the strength. Fu's model describes a fiber efficiency factor of 56 % for a mean fiber length of 250 μm. At 125 μm, this drops to 36 % and at 62.5 μm to even less than 20 %. Thus, fiber shortening that can ranges between 1.2 and 14.4 % in FFF reduces the mechanical performance[44].

During the feedstock material production for FFF, the short fibers are aligned along the pull-off axis. Moreover, the orientation and the enclosed pores are different for different feedstock materials, producers and production types[45,46]. This effect also holds true in the extrusion nozzle of the printer[5]. For the redirection of the extrusion thread onto the build plate, a deflection of 90 ° is applied. This results in different turning radii within the thread. The different velocities on the top and bottom side of the thread change the fiber orientation during lay-up[47,48]. Nevertheless, the general orientation in the direction of the thread deposition is detectable in the printed material[49]. Several research groups have already investigated the fiber orientation as a function of the nozzle geometry for mass-produced polymers[49–51].

In the standardized design of a print head, the heat-break separates the heated section (hot-end) from the rest of the assembly. Within the hot-end, the nozzle is butt-jointed with the heat-break. This does not pose a problem for industrial use. For medical applications, the cleanness of the deposited material has to be ensured. The use of uninterrupted nozzles without joints or undercuts makes this possible. To generate a continuous nozzle, the entire channel and nozzle angle has to be generated in one step. This requires bore depths of more than 60 mm. The generation of a uniform inner surface of the barrel and nozzle angle is a challenging task and has barely been investigated.

In this report, we introduce a custom-made nozzle design. This design consists of an uninterrupted nozzle channel without joints (cold-end + heat-break + hot-end in one piece) for an improved flow behavior. Besides the overall design, it allows the production of individual inner nozzle shapes. The focus is on the influence of the fiber formation of short carbon fiber reinforcements. This is investigated with the high-performance polymer PEEK as a matrix material.

MATERIALS AND METHODS

The investigation within this study is performed with cuboidal samples. The size of the samples is 4 mm × 10 mm × 40 mm. The slicing software Simplify3D generates the print code (G-code). Printing of five threads as brim (contour layers placed around the first layer of the part) ensures the stability of the process. Print path of the samples is unidirectional along the longitudinal axis. Exceptions are the turning points at the front sides.

For better adhesion on the build plate, a thin film of Dimafix® is used. The print bed is preheated and levelled to 0.1 mm distance from nozzle with a feeler gauge before printing. Before printing, the feedstock material is dried at 70 °C in an oven.

Materials and Equipment

The print material is Victrex 450G with 30 % carbon fiber content by weight[10]. The feedstock material is a filament produced by Ensinger GmbH. This material is a derivative of PEEK and therefore belongs to the group of high-performance thermoplastics.

The applied printer is an Apium P220. This printer works with a Cartesian movement system. The maximum print speed is limited to less than 100 mms^{-1}. For the standard version, the maximum build plate temperature is 160 °C. The adjustable extrusion temperature is more than 500 °C.

The print head structure enables the use of an uninterrupted nozzle. Thus, the nozzle design combines the hot-end and cold-end in one piece. The hot-end side has an M8 thread and the cold-end a transition tolerance of 6 mm. A uniform adapter allows the mounting of custom-made nozzles. The front part made of stainless steel enables the fit in the thread. A clamping ring of brass ensures conductivity in the end of the front part at the edge of the heat break. The back part is a sleeve made of brass. This ensures the cooling of the entering filament in the backside. This setup with a custom-made nozzle is shown in Fig. 2.

The developed method for the production of nozzles allows an almost unlimited design of the inner geometry. The present investigation includes three different nozzle angles. One is the nozzle standard of 120 °. For the investigation of the flow profile, angles of 90 ° and 60 ° are additionally included. Figure 3 shows the tip design of the custom-made nozzles. The nozzle outlet of all variants is designed with a diameter of 0.4 mm.

Analytical Methods

Using a Keyence VR5200 profilometer allows the calculation of the surface coordinates with an accuracy of approx. 0.5 μm. For microscopic images, the samples are cut in half and embedded in epoxy resin. The samples are ground and polished with a polish suspension that contains particles up to a size of 1 μm. Using a light microscope (Olympus BX41) in reflection mode provides images
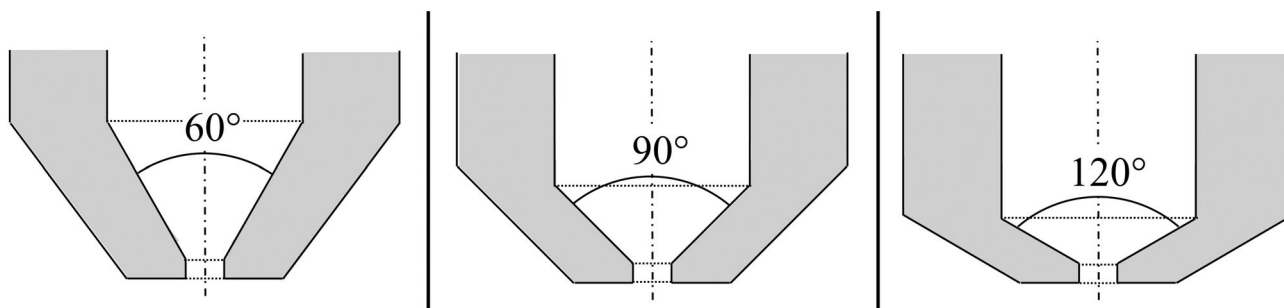
Figure 3. Custom-made and investigated nozzle angles.

for analytical examination. The images are analyzed with Olympus Stream Motion software and its optical filters.

RESULTS

In the first step, the custom-made nozzles are investigated. These, as well as the reference, have an uninterrupted nozzle design. The geometric differences from the reference nozzle and the possible benefits associated with the custom-made nozzles are shown. Upon optimization of the process parameters, samples for fiber formation analysis are generated. The analysis of the printed material includes both orientation and length of the fibers.

Nozzle Geometry and Shape

The shape of the nozzle tip and the diameter of the outlet opening define the thread line. The quality of the inner surface is a crucial quality feature in a nozzle channel. The developed manufacturing process does not require machining of the entire channel. This manufacturing approach allows a different definition of the characteristic length of the outlet L_3. Therefore, the diameter and the characteristic of the outlet are further analyzed.

Nozzle Tip and Diameter

A drill hole creates the nozzle outlet. This is done from the front end of the nozzle. Due to the alignment tolerances, centric drilling into the previously manufactured nozzle tip can be difficult depending on the length of the nozzle channel. A non-coaxial alignment of the outlet and the channel results in undercuts inside the nozzle that will cause irregularities in the flow profile. The results are additional dead water areas. Figure 4 shows a tolerance-related offset of the nozzle outlet hole with respect to
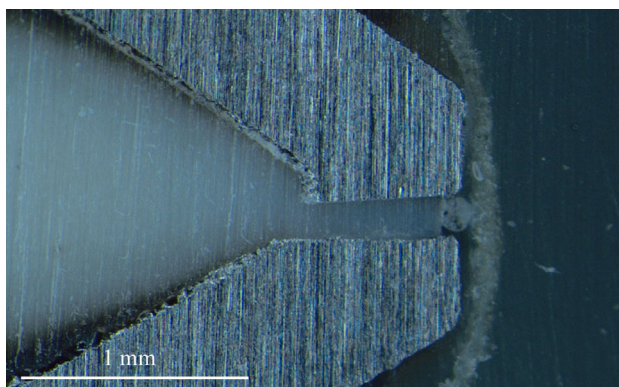

Figure 4. Nozzle tip of uninterrupted reference nozzle.

the channel of the reference nozzle and the undercut caused by this.

Additional measuring levels in the developed manufacturing process of the custom-made nozzles ensure the coaxiality of the outlet and the channel. This prevents the occurrence of undercuts inside the nozzle. One consequence is an imbalance in the material. The creation of the outlet can cause edge chipping and structural anomalies. Figure 5 shows examples of these phenomena.

The standard nozzle diameter for FFF printers is 0.4 mm. The engineering fit for the outlet is H10. This is equal to a tolerance of +40 µm, which equates to +10 % here. The diameters of the manufactured nozzles are 3.5–8 % above the targeted size. Table 1 presents the detailed results. This way the variation is not outside the usual market tolerance range. The measured reference nozzle shows a variation of 3 %.

Inner Surface Quality

The processing of PEEK requires heating above the melting temperature. The basic compound 450G has a melting point of 343 °C[10]. Extrusion temperatures of 400 °C or higher are used in well-known research work of additive manufacturing[52, 53, 6]. These temperatures also affect the high-performance thermoplastic PEEK during extended exposure. Adhesions on the surface of the nozzle channel can degrade during longer exposure times. For this reason, not only the nozzle outlet, but also the surface of the entire inner barrel is a quality criterion. The investigation of these surfaces is performed on a longitudinal section of the nozzles. The measured section is a 4 mm long section of the inner surface, which is parallel to the longitudinal axis. The visual measurement of the surfaces for a custom-made and a reference nozzle is shown in Fig. 6. A qualitative evaluation of the optically recognizable topology shows larger amplitudes of the notches for the reference nozzle. Figure 7 shows the detectable height profiles of the reference and the custom-made nozzles.

The arithmetic average for surface roughness is R_a. This is 2.6 µm for the custom-made design and 2.2 µm for the reference nozzle. On average, the surface topologies are approximately comparable for the measured distance of 4 mm. The roughness depth R_z is the average value of the maximum height differences in five connected individual sections. This value is an indication for the fluctuation in the height profile. R_z is 13.6 µm for the custom-made design and 30.9 µm for the reference nozzle. The fluctuations in the height profile are greater for the reference nozzle. For a more detailed analysis, the entire measuring section is subdivided into 18.47 µm long sections. The maximum height difference within these sections is 3.93 µm for the custom-made design. For the reference nozzle, more than 19 % of the
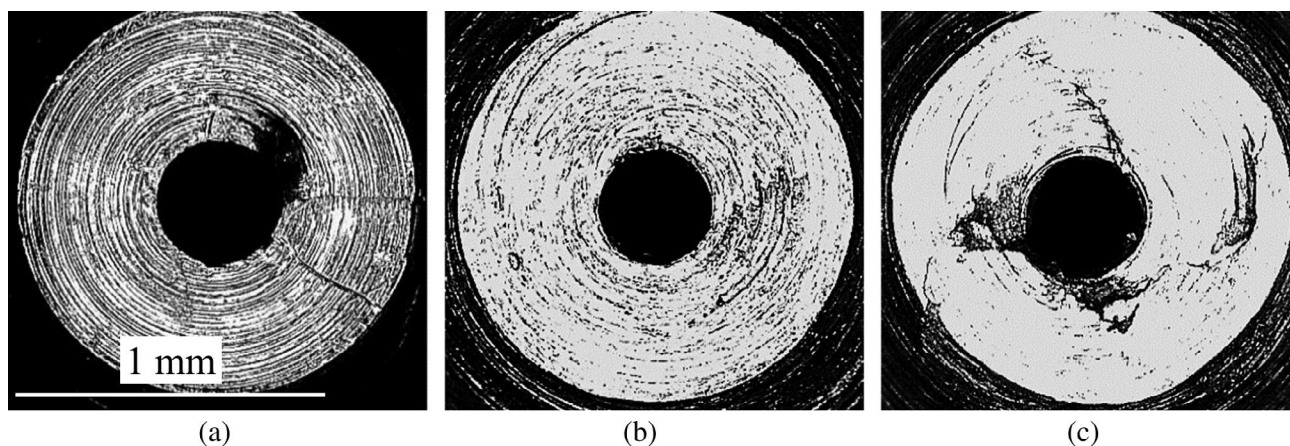
Figure 5. Top view of the nozzle tip of the custom-made design: (a) with breakout, (b) concentric and (c) with structural anomalies.

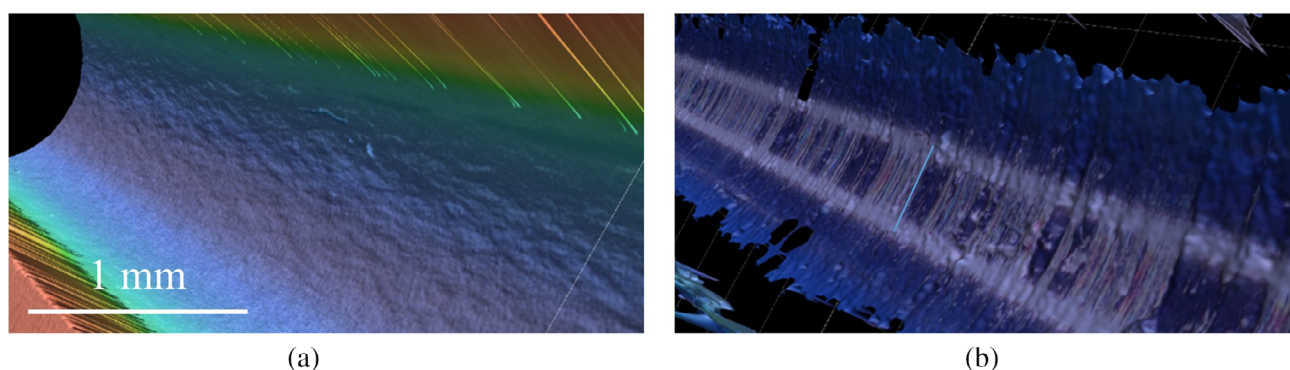| Table 1. Diameter of the new design				
Nozzle angle (°)	60	90	120	Reference
Diameter (µm)	435	432	414	412
Deviation (%)	8.8	8	3.5	3

Figure 6. Visualization of inner surface: (a) custom-made design; (b) reference.

sections have a larger height difference. Here, the maximum height within a section is over 13 µm. This is more than three times great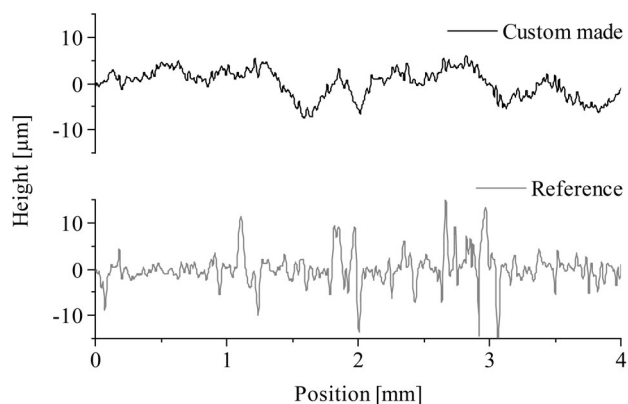er than that for the custom-made design, which measurably has a more uniform surface texture. This reduces the probability of material accumulation in the notches. Therefore, the probability of nozzle clogging can be reduced with the custom-made design.

Nozzle Length Value L_3

The value L_3 is the length of the reduction channel. As previously mentioned, a standard ratio of length to diameter is *approx.* 1.5 (L_3/D_2). With a profilometer and at an orientation angle β, L_3 can be optically detected from the nozzle tip. The measurements are made at $\beta = 50$ °. Each nozzle is measured three times. Between the measurements, the nozzle is rotated by 120 °. This way the circumferential symmetry can be mapped (Fig. 8).

Table 2 lists the measured results. With a target value of 200 µm, the channels are on average about 5.5–9.5 % longer. The targeted ratio is 0.5 (L_3/D_2). The geometric ratio of the custom-made nozzles is 0.49–0.52 on average. Despite the individual tolerance ranges, the desired geometric behavior of the nozzles is achieved.
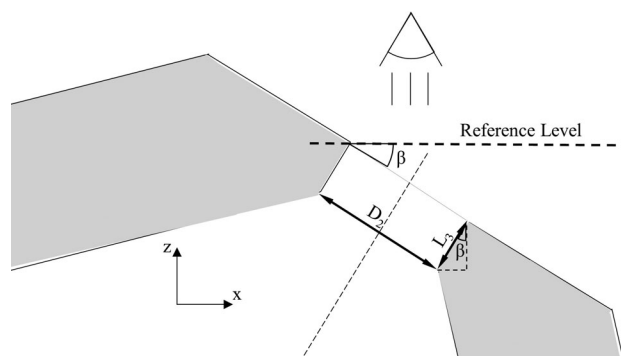

Figure 7. Measurements of inner nozzle surface.

Figure 8. Geometric correlation of dimensions at the tip of the nozzle.

Table 2. L_3 and fiber orientation of the new design

Nozzle angle (°)	60	90	120
L_3 (μm)	211 (±25)	219 (±36)	217 (±16)
Deviation to 200 μm (%)	5.5	9.5	8.5
Geometric ratio (L_3/D_2)	0.49	0.51	0.52
Transversely oriented fibers (%)	20.6 (±4.2)	30.8 (±2.2)	28.6 (±6.7)
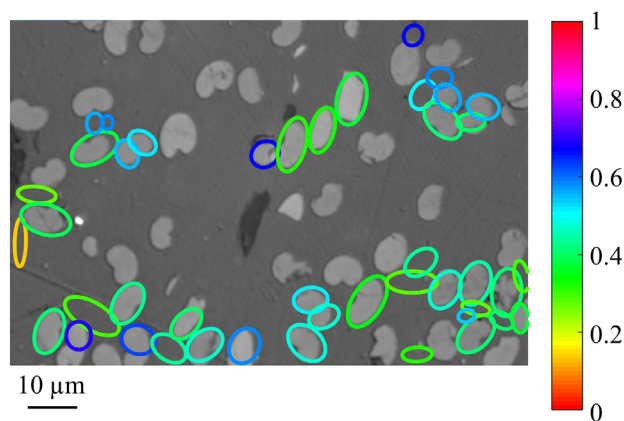
Figure 9. Distribution of 'out-of-plane angle' of reinforcing fibers.

Figure 10. Distribution of fiber length in printed samples.
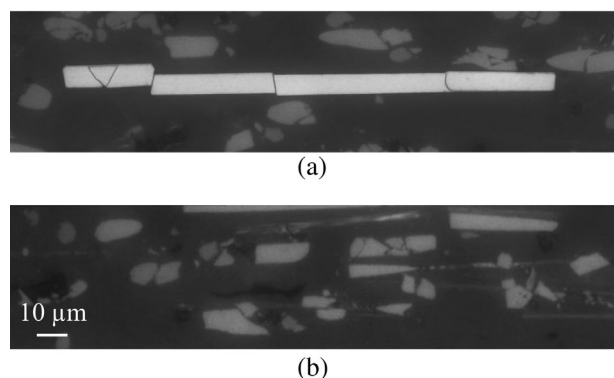
Figure 11. (a) Connected multiple broken fiber. (b) Fiber fragments without a connected arrangement.

The geometrical relations of the custom made nozzles are comparable.

Fiber Formation

Fiber formation is determined by fiber orientation and length. Both properties define the mechanical performance of a printed part. Depending on the application, the orientation through the extrusion process conflicts with the requirement profile with regard to isotropy. This can be influenced by changing the flow profile in the nozzle. A lower alignment, however, can result in an excessive shortening of the fibers during deposition.

Orientation

In a cross-sectional cut, the fibers are circular. With increasing orientation angle from the 0° plane, the fibers form an ellipse. By measuring the ellipse, the alignment angle with respect to the cut plane ca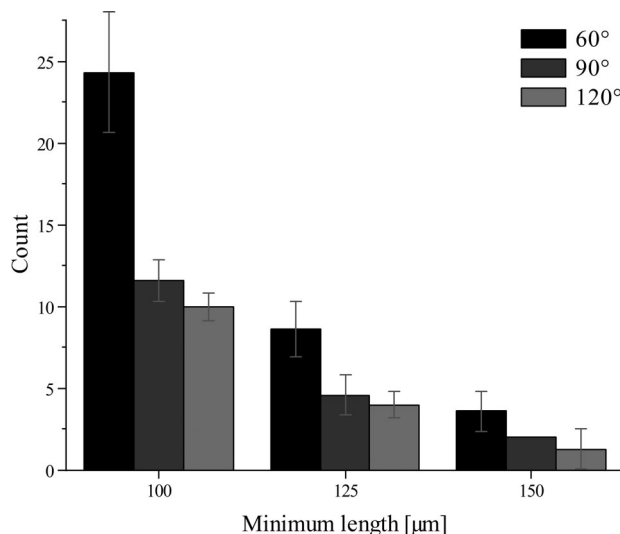n be calculated. Eberl[54] presents an evaluation tool for this purpose. This tool recognizes the elliptical shape and colors it depending on the alignment. In case of a cross-sectional cut and an associated circular shape, the form factor of the investigated fiber is 1. Figure 9 shows an example of a measurement.

The detectable fiber cross-sections are neither round nor elliptical. Instead, the profile is bean-shaped. This fiber cross-section can result from the manufacturing process[55,56]. To obtain an estimate of the frequency of non-circular fiber cross-sections, a phase analysis is performed. A form factor of 0.75 is defined as the threshold value. If an element has a form factor greater than 0.75, it is a fiber with a circular cross-section. Eighteen micrographs with an average of 215 objects recognized as fiber are analyzed. The relative amount of circular fibers is 13 %. The measurement of the fiber orientation with the presented algorithm is not possible.

The determination of the longitudinal alignment of the fibers is possible by analyzing the transversely aligned fibers. A longitudinal section allows the analysis of the transversely oriented fibers. A fiber is considered as transversely oriented if the perimeter of the fiber's cross-section is smaller than 50 μm. The cross-sectional areas of these fibers are summarized and set into relation with the total area of the investigated section. The results in Table 2 represent the average of three images.

Length

The measurement of the fiber length distribution is based on sample cuts in the longitudinal direction. All areas greater than 500 μm^2 are defined as a measurable fiber. The number of fibers per image with a minimum length of 100, 125 and 150 μm is determined. Only fibers that do not show any breaks or cracks are counted. Per sample, images are taken at three different locations and the results are averaged. Figure 10 illustrates the result of this investigation. It can be seen that the number of fibers for the given lengths decreases with increasing nozzle angle.

The fiber length is directly related to the occurrence of fiber breaking due to interactions in the melt flow. Different types are detectable. Figure 11 shows a multiple broken fiber. The total length is 160 μm with a total of five breaks. The individual fracture surfaces of the fiber are directly adjacent to each other. The fragments are offset at the fracture surfaces transverse to the fiber direction. The figure also shows broken fiber pieces. However, these do not show any connected formation. The fragments are of different sizes, between 5 to 60 μm.

DISCUSSION

PEEK is one of the few polymers that meet the requirements for aviation[57], aerospace[58] and medical applications[59]. PEEK is particularly suitable for the medical sector, especially for implants, and is increasingly in demand[60].

Additive manufacturing addresses these sectors, that are characterized through the application of custom-made parts. Nevertheless, insufficient process stability prevents a widespread additive manufacturing of high-performance polymers like PEEK. As with low-cost printers, nozzle clogging is the primary process failure when processing high-temperature polymers. Previous research groups have identified the quality of the inner nozzle surface as critical to the extrusion stability[30,37–39]. Both the custom-made and reference nozzles show a similar arithmetic average for surface roughness. The roughness depth of the custom-made nozzle is one-third of that of the reference nozzle in a detailed examination. This prevents the polymer melt from adhering to the inner surface of the custom-made nozzle. A 3D print usually takes over several hours. PEEK begins to degrade at temperatures above 400 °C after less than an hour[61]. As a result, the probability of nozzle clogging can be considerably reduced by a decreasing of the profile depth.

Sharma et al.[62] provide evidence of the possible applications of printed implants. Further research on reproducibility and biomechanical behavior and guidelines is necessary. Vaezi and Yang[63] identified contamination of the material during the process as critical in this context. The presented custom-made nozzle is able to close this leak with a consistent quality.

The analysis of fiber orientation indicates an increase with decreasing nozzle angle. For a 60 ° nozzle angle, the detectable area of irregularly oriented fibers makes up 20.6 % of the investigated area. This ratio increases for larger nozzle angles. At the transition from the convergence zone to the nozzle outlet, the fibers must be deflected to different degrees. The more strongly the fibers have to be deflected, the more the resulting fiber orientation deviates from the extrusion direction. This confirms the presented results. Heller et al.[51] modeled the fiber orientation as a function of the nozzle angle and found only a slight influence of the angle. This modeling postulates a fiber orientation in the

direction of extrusion with increasing nozzle angle. Therefore, in addition to the present results, the relationship between nozzle angle and orientation has to be investigated.

Besides the orientation, fiber length is even more important for short-fiber reinforcemnts[43]. The technical data for short-fiber-reinforced PEEK from injection-molded specimens meet these requirements[10]. However, additively manufactured specimens do not meet them. The strength is 39 % and the modulus of elasticity 29.6 % of the characteristic values for injection molding[10,52]. These results imply excessive shortening of the fibers caused by the process. The fiber length distribution shows a clear correlation regarding the nozzle angle. With increasing nozzle angle, the number of fibers of a certain minimum length decreases. With increasing nozzle angle, the flow profile in the conical part is changed. The fluid elements lift off the inner wall of the barrel and the fiber interactions increase. Furthermore, in the 120 ° nozzle, the melt hits the nozzle wall at a steeper angle, which means that the fibers have to be strongly deflected. The advantage with respect to the flow profile outweighs the disadvantageous characteristics of friction loss, shear stress and pressure drop.

The reference nozzle was also found to have a non-coaxial alignment of the outlet and the nozzle channel. The resulting undercuts cause irregularities in the melt flow and dead water zones that have negative effects on the total fiber formation. This problem is not found in the developed manufacturing of the custom-made nozzles.

CONCLUSIONS AND OUTLOOK

The focus of this paper is the investigation of an uninterrupted nozzle system for the printing of the high-performance thermoplastic PEEK with short fiber reinforcement. A custom-made nozzle concept with variable outlet angle is presented and the achievable fiber length distribution and fiber orientation in the printed material are investigated.

A characterization of the nozzles is done by comparison with a reference. The segmented nozzle surface of the custom-made nozzles shows a maximum roughness of $R_z = 3.93$ μm. The reference nozzle has a maximum of about 13 μm. The outlet shapes of both nozzle concepts are comparable; however, the coaxiality of the outlet and the channel for the custom-made nozzles is ensured.

It can be demonstrated that a smaller nozzle angle decreases the amount of damage added to the fibers during deposition. Thus, the shortening of the fibers by the process is reduced. A clear result for the fiber orientation cannot be deduced. The bean shape of the fibers prevents an optical analysis. In a further procedure, the presented analysis tool has to be adapted according to the descriptions of Sharp et al.[55] The analysis of the fiber orientation using a micro-computed tomography is of further interest. According to Heller et al.[51], the reduction channel length L_3 has a greater influence on the fiber orientation than the nozzle angle. The degree of orientation in the extrusion direction decreases with an increasing length L_3. Therefore, further test specimens with a modified L_3 have to be produced and analyzed.

Finally, the advantages of the nozzle system and the investigations of the nozzle angle under real conditions have to be determined. The test setup presented by Matschinski et al.[64] is used for this purpose. In this context, inline measuring systems are to be used for a further detailed investigation[65].

AUTHOR CONTRIBUTIONS

AM and TA conceived of the presented idea. AM encouraged PZ to investigate the fiber formation and supervised the findings of this work. AM encouraged TW to investigate the general nozzle design and supervised the findings of this work. AM wrote the manuscript with support from PZ. All authors discussed the results and contributed to the final manuscript.

CONFLICTS OF INTEREST

None.

ACKNOWLEDGEMENTS

REFERENCES

1 Wohlers T, *Wohlers Report: 3D Printing and Additive Manufacturing State of the Industry*. Wohlers Associates, Fort Collins, CO (2018).
2 Küpper D, Heising W, Corman G, Wolfgang M, Knizek C, Lukic V. Get Ready for Industrialized Additive Manufacturing (2017). Available: https://www.bcg.com/de-de/publications/2017/lean-manufacturing-industry-4.0-get-ready-for-industrialized-additive-manufacturing.aspx [16 January 2020].
3 Türk D-A, Kussmaul R, Zogg M, Klahn C, Leutenecker-Twelsiek B and Meboldt M, *Procedia CIRP* **66**:306–311 (2017). https://doi.org/10.1016/j.procir.2017.03.359.
4 Luo M, Tian X, Shang J, Zhu W, Li D and Qin Y, *Composites A* **121**:130–138 (2019). https://doi.org/10.1016/j.compositesa.2019.03.020.
5 Ngo TD, Kashani A, Imbalzano G, Nguyen KTQ and Hui D, *Composites B* **143**:172–196 (2018). https://doi.org/10.1016/j.compositesb.2018.02.012.
6 Rinaldi M, Ghidini T, Cecchini F, Brandao A and Nanni F, *Composites B* **145**:162–172 (2018). https://doi.org/10.1016/j.compositesb.2018.03.029.
7 Haleem A and Javaid M, *Clin Epidemiol Global Health* **7**:571–577 (2019). https://doi.org/10.1016/j.cegh.2019.01.003.
8 Kang J, Wang L, Yang C, Wang L, Yi C, He J *et al.*, *Biomech Model Mechanobiol* **17**:1083–1092 (2018). https://doi.org/10.1007/s10237-018-1015-x.
9 Wang L, Huang L, Li X, Zhong D, Li D, Cao T *et al.*, *Ann Thorac Surg* **107**:921–928 (2019). https://doi.org/10.1016/j.athoracsur.2018.09.044.
10 Victrex. PEEK 450G/450CA30 Data Sheet (2019).
11 Reilly DT and Burstein AH, *J Biomech* **8**:393–405 (1975). https://doi.org/10.1016/0021-9290(75)90075-5.
12 Rho JY, Ashman RB and Turner CH, *J Biomech* **26**:111–119 (1993). https://doi.org/10.1016/0021-9290(93)90042-D.
13 Yan M, Tian X, Peng G, Li D and Zhang X, *Compos Sci Technol* **165**:140–147 (2018). https://doi.org/10.1016/j.compscitech.2018.06.023.
14 Papageorgiou DG, Liu M, Li Z, Vallés C, Young RJ and Kinloch IA, *Compos Sci Technol* **175**:60–68 (2019). https://doi.org/10.1016/j.compscitech.2019.03.006.
15 Mulholland T, Goris S, Boxleitner J, Osswald T and Rudolph N, *J Compos Sci* **2**:45 (2018). https://doi.org/10.3390/jcs2030045.
16 Turner BN, Strong R and Gold SA, *RPJ* **20**:192–204 (2014). https://doi.org/10.1108/RPJ-01-2013-0012.
17 Tlegenov Y, Lu WF and Hong GS, *Prog Addit Manuf* **4**:211–223 (2019). https://doi.org/10.1007/s40964-019-00089-3.
18 Bellini A, Güceri S and Bertoldi M, *J Manuf Sci Eng* **126**:237–246 (2004). https://doi.org/10.1115/1.1688377.
19 Phan DD, Horner JS, Swain ZR, Beris AN and Mackay ME, *Addit Manuf* **33**:101161 (2020). https://doi.org/10.1016/j.addma.2020.101161.
20 Toschi F and Sega M, *Flowing Matter*. Springer International Publishing, Cham (2019).
21 Gibson AG and Williamson GA, *Polym Eng Sci* **25**:980–985 (1985). https://doi.org/10.1002/pen.760251511.
22 Michaeli W, *Extrusion Dies for Plastics and Rubber: Design and Engineering Computations*, 2nd revised edn. Hanser/Oxford University Press, Munich (1992).
23 Yardimci MA, Guceri SI, Danforth SC. Thermal Analysis of Fused Deposition. Solid Freeform Fabrication Symposium, Austin (1997). Available: http://utw10945.utweb.utexas.edu/Manuscripts/1997/1997-80-Yardimci.pdf [19 September 2020].
24 Bellini A. Fused deposition of ceramics: a comprehensive experimental, analytical and computational study of material behavior, fabrication process and equipment design. Doctoral thesis, Drexel University (2002).
25 Ramanath HS, Chua CK, Leong KF and Shah KD, *J Mater Sci Mater Med* **19**:2541–2550 (2008). https://doi.org/10.1007/s10856-007-3203-6.
26 Go J, Schiffres SN, Stevens AG and Hart AJ, *Addit Manuf* **16**:1–11 (2017). https://doi.org/10.1016/j.addma.2017.03.007.
27 Vergnes B, *Int Polym Process* **30**:3–28 (2015). https://doi.org/10.3139/217.3011.
28 Mompean G and Deville M, *J Non-Newtonian Fluid Mech* **72**:253–279 (1997). https://doi.org/10.1016/S0377-0257(97)00033-5.
29 Liang J-Z, *J Mater Process Technol* **52**:207–212 (1995). https://doi.org/10.1016/0924-0136(94)01610-D.
30 Agassant J-F, Arda DR, Combeaud C, Merten A, Münstedt H, Mackley MR *et al.*, *Int Polym Process* **21**:239–255 (2006). https://doi.org/10.3139/217.0084.
31 Akhtar SS and Arif AFM, *J Fail Anal Prev* **10**:38–49 (2010). https://doi.org/10.1007/s11668-009-9304-4.
32 Fallon JJ, McKnight SH and Bortner MJ, *Addit Manuf* **30**:100810 (2019). https://doi.org/10.1016/j.addma.2019.100810.
33 Ivanova O, Williams C and Campbell T, *Rapid Prototyping J* **19**:353–364 (2013). https://doi.org/10.1108/RPJ-12-2011-0127.
34 Wang X, Jiang M, Zhou Z, Gou J and Hui D, *Composites B* **110**:442–458 (2017). https://doi.org/10.1016/j.compositesb.2016.11.034.
35 Beran T, Mulholland T, Henning F, Rudolph N and Osswald TA, *Addit Manuf* **23**:206–214 (2018). https://doi.org/10.1016/j.addma.2018.08.009.
36 Wittbrodt BT, Glover AG, Laureto J, Anzalone GC, Oppliger D, Irwin JL *et al.*, *Mechatronics* **23**:713–726 (2013). https://doi.org/10.1016/j.mechatronics.2013.06.002.
37 Chen Y, Kalyon DM and Bayramli E, *J Appl Polym Sci* **50**:1169–1177 (1993). https://doi.org/10.1002/app.1993.070500707.
38 Kissi NE, Léger L, Piau J-M and Mezghani A, *J Non-Newtonian Fluid Mech* **52**:249–261 (1994). https://doi.org/10.1016/0377-0257(94)80054-5.
39 Arda DR and Mackley MR, *J Non-Newtonian Fluid Mech* **126**:47–61 (2005). https://doi.org/10.1016/j.jnnfm.2004.12.005.
40 Ning F, Cong W, Qiu J, Wei J and Wang S, *Composites B* **80**:369–378 (2015). https://doi.org/10.1016/j.compositesb.2015.06.013.
41 Fu S-Y, Lauke B, Mäder E, Yue C-Y and Hu X, *Composites A* **31**:1117–1125 (2000). https://doi.org/10.1016/S1359-835X(00)00068-3.
42 Ferreira I, Machado M, Alves F and Torres Marques A, *Rapid Prototyping J* **25**:972–988 (2019). https://doi.org/10.1108/RPJ-01-2019-0004.
43 Fu S-Y and Lauke B, *Compos Sci Technol* **56**:1179–1190 (1996). https://doi.org/10.1016/s0266-3538(96)00072-3.
44 Jiang D and Smith DE, *Addit Manuf* **18**:84–94 (2017). https://doi.org/10.1016/j.addma.2017.08.006.
45 Sommacal S, Kingston A, Ploeckl M, Matschinski A, Consul P, Saadatfar M et al. 3D characterisation of carbon fibre reinforced composite microstructure via X-ray computed tomography. International Conference on Composite Materials (ICCM22), Melbourne (2019). Available: http://iccm22.com/.
46 Sommacal S, Matschinski A, Drechsler K, Compston P. CF/PEEK 3D printed materials microstructure characterisation by X ray computed tomography. SAMPE Europe, Amsterdam (2020). Available: https://www.sampe-europe.org/.
47 Tekinalp HL, Kunc V, Velez-Garcia GM, Duty CE, Love LJ, Naskar AK *et al.*, *Compos Sci Technol* **105**:144–150 (2014). https://doi.org/10.1016/j.compscitech.2014.10.009.
48 Brenken B, Barocio E, Favaloro A, Kunc V and Pipes RB, *Addit Manuf* **21**:1–16 (2018). https://doi.org/10.1016/j.addma.2018.01.002.
49 Hofstätter T, Gutmann IW, Koch T, Pedersen DB, Tosello G, Heinz G et al. Distribution and orientation of carbon fibers in polylactic acid parts

produced by fused deposition modeling. Proceedings of ASPE Summer Topical Meeting (2016).

50 Papon EA, Haque A and Sharif MAR, *Effect of Nozzle Geometry on Melt Flow Simulation and Structural Property of Thermoplastic Nanocomposites in Fused Deposition Modeling*. DEStech Publications, Lancaster, PA (2017).

51 Heller BP, Smith DE and Jack DA, *Addit Manuf* **25**:227–238 (2019). https://doi.org/10.1016/j.addma.2018.10.031.

52 Han X, Yang D, Yang C, Spintzyk S, Scheideler L, Li P *et al.*, *J Clin Med* **8** (2019). https://doi.org/10.3390/jcm8020240.

53 Arif MF, Kumar S, Varadarajan KM and Cantwell WJ, *Mater Des* **146**: 249–259 (2018). https://doi.org/10.1016/j.matdes.2018.03.015.

54 Eberl LM, *Mechanical Performance of Pinned Composite/Metal Joints under Tension. 1. Auflage*. Verlag Dr. Hut, München (2019). (Lehrstuhl für Carbon Composites, Fakultät für Maschinenwesen, Technische Universität MünchenBand 54 (2018)).

55 Sharp N, Goodsell J and Favaloro A, *J Compos. Sci* **3**:23 (2019). https://doi.org/10.3390/jcs3010023.

56 Alcalá-Sánchez D, Tapia-Picazo J-C, Bonilla-Petriciolet A, Luna-Bárcenas G, López-Romero JM and Álvarez-Castillo A, *Int J Polym Sci* **2020**:1–13 (2020). https://doi.org/10.1155/2020/8029516.

57 Grünewald J, Parlevliet PP, Matschinski A and Altstädt V, *J Sandwich Struct Mater.* **21**:2680–2699 (2019). https://doi.org/10.1177/1099636217715704.

58 May R, Polyetheretherketones, in *Encyclopedia of Polymer Science and Technology*. John Wiley, Hoboken, NJ, p. 2362 (2002).

59 Panayotov IV, Orti V, Cuisinier F and Yachouh J, *J Mater Sci Mater Med* **27**:118 (2016). https://doi.org/10.1007/s10856-016-5731-4.

60 Kurtz SM and Devine JN, *Biomaterials* **28**:4845–4869 (2007). https://doi.org/10.1016/j.biomaterials.2007.07.013.

61 Cole KC and Casella IG, *Polymer* **34**:740–745 (1993). https://doi.org/10.1016/0032-3861(93)90357-G.

62 Sharma N, Aghlmandi S, Cao S, Kunz C, Honigmann P and Thieringer FM, *J Clin Med* **9**:2818 (2020). https://doi.org/10.3390/jcm9092818.

63 Vaezi M and Yang S, *Virtual Phys Prototyping* **10**:123–135 (2015). https://doi.org/10.1080/17452759.2015.1097053.

64 Matschinski A, Juan Alburquerque A, Kriegl B, Drechsler K. Development of a Test Bench for Fused Filament Fabrication. The Composites and Advanced Materials Expo, Orlando (2020).

65 Matschinski A. Additive manufacturing. European Patent EP3587077